Published in
Physical Review A 76, issue 2, 023407 1-10, 2007
which should be used for any reference to this work



# Sensitivity of double-resonance alignment magnetometers

Gianni Di Domenico,* Hervé Saudan, Georg Bison, Paul Knowles, and Antoine Weis
*Physics Department, University of Fribourg, Chemin du Musée 3, 1700 Fribourg, Switzerland*

We present an experimental study of the intrinsic magnetometric sensitivity of an optical or rf-frequency double-resonance magnetometer in which *linearly* polarized laser light is used in the optical pumping and detection processes. We show that a semiempirical model of the magnetometer can be used to describe the magnetic resonance spectra. Then, we present an efficient method to predict the optimum operating point of the magnetometer, i.e., the light power and rf Rabi frequency providing maximum magnetometric sensitivity. Finally, we apply the method to investigate the evolution of the optimum operating point with temperature. The method is very efficient to determine relaxation rates and thus allowed us to determine the three collisional disalignment cross sections for the components of the alignment tensor. Both first and second harmonic signals from the magnetometer are considered and compared.

## I. INTRODUCTION

Our group develops optically pumped alkali-metal-atom vapor magnetometers (OPM) for both applied [1] and fundamental [2] research. The diverse requirements of these demanding applications, in terms of sensitivity, spatial resolution, scalability, and measurement bandwidth, warrants investigation of new OPM schemes. An interesting and promising avenue is the use of atomic *alignment* instead of *orientation* to probe the external magnetic field. We will refer to an OPM based on atomic alignment as DRAM (double-resonance alignment magnetometer), while we will speak of DROM (double-resonance orientation magnetometer) when the magnetization has the symmetry of an atomic orientation. Recently, our group presented both theoretical [3] and experimental [4] investigations of the magnetic resonance spectra produced in a cesium vapor in which an alignment is created and detected by a single linearly polarized laser beam.

Of direct importance for us, the DRAM scheme has a more flexible geometry than the well-known DROM $M_x$ configuration [5]. For maximal sensitivity, the DROM scheme requires a 45° angle between the laser beam and the magnetic field [5], limiting applications calling for a compact arrangement of multiple sensors. In multichannel devices, as required for cardiomagnetic measurements [6] for example, the DRAM method offers the advantage that the laser beam can be oriented either parallel or perpendicular to the offset field without loss of sensitivity.

The line shapes of the second harmonic DRAM signal have significantly narrower linewidths than the DROM signal under identical conditions. Narrow linewidths suppress systematic errors in optical magnetometers, visible as long term baseline drifts, and potentially increase the magnetometric sensitivity. This means that a DRAM could lead to a higher magnetometric sensitivity than a DROM for equal signal to noise ratio.

Moreover, in DROM devices the interaction of the atoms with the circularly polarized laser light leads to an $M$ dependent energy shift of the Zeeman hyperfine components when the laser frequency is not centered on the optical resonance line, the so-called light shift [7,8]. In that case, the effect of laser power and frequency changes is indistinguishable from the effect of magnetic field changes, thus limiting the magnetometric performance and introducing systematic uncertainties on the determination of the absolute value of the field. In the DRAM, the linearly polarized light produces a light shift depending on $M^2$, which does not have the same characteristics as a magnetic field Zeeman interaction. The $M^2$ shift broadens the magnetic resonance line, thereby slightly reducing the magnetic sensitivity, but it will not shift the resonance frequency. The absence of linear $M$-dependent systematic resonance shifts make the DRAM an attractive magnetometer for precision experiments searching for $M$-dependent effects, such as electric dipole moment searches [9].

In this article, we present an experimental study of the magnetometric sensitivity of a double-resonance alignment magnetometer. The principle of the DRAM with its theoretical description is given in Sec. II, the experimental setup is described in Sec. III, and the operational definition of the magnetometric sensitivity is introduced in Sec. IV. Then, in Sec. V we show that a simple empirical extension of the DRAM model extends its validity to significantly higher laser powers. This extended model is used in Sec. VI, where we develop a method to predict the optimum operating point of the DRAM based on physical parameters extracted from specific measurements. Finally, the method is applied in Sec. VII to determine the temperature dependence of the DRAM optimum operating point, and the results obtained for different cells are compared in Sec. VIII.

## II. DOUBLE-RESONANCE ALIGNMENT MAGNETOMETER

The geometry of a double-resonance alignment magnetometer is presented in Fig. 1: It is identical to the one described in [3]. A linearly polarized laser beam, with polarization $\boldsymbol{\epsilon}$ inclined at angle $\gamma$ to the magnetic field to be measured, $\boldsymbol{B}_0$, is used to create an atomic alignment via op-

*Gianni.DiDomenico@unifr.ch

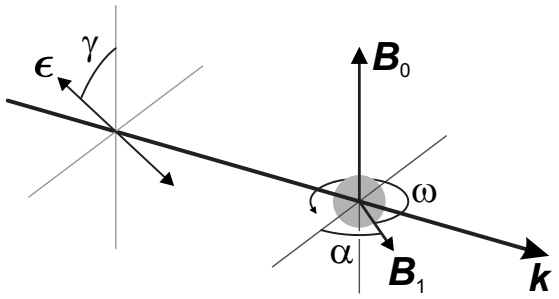


FIG. 1. Double-resonance magnetometer geometry using linearly polarized light. Here, $\boldsymbol{k}$ is the direction of the linearly polarized laser beam. The rf field $\boldsymbol{B}_1$ (shown here at $t=0$) rotates in a plane perpendicular to the static field $\boldsymbol{B}_0$. The linear polarization vector $\boldsymbol{\epsilon}$ makes an angle $\gamma$ with the static field $\boldsymbol{B}_0$, and the phase of $\boldsymbol{B}_1$ is characterized by $\alpha$.

tical pumping in a room temperature vapor of cesium atoms. This alignment precesses under the simultaneous action of the static magnetic field $\boldsymbol{B}_0$ and a much weaker magnetic field $\boldsymbol{B}_1$, called the rf field, rotating at frequency $\omega$ in the plane perpendicular to $\boldsymbol{B}_0$ and driving the magnetic resonance transitions. Competition between relaxation, optical pumping, and magnetic resonance produces a steady state in the rotating frame.

The precession of the alignment generates modulations of the absorption coefficient which create signals at both the fundamental ($\omega$) and the second harmonic ($2\omega$) of the applied rf frequency $\omega$. The magnetic resonance signals $S_\omega(t)$ and $S_{2\omega}(t)$ are obtained here by monitoring the transmitted light power with a photodiode. A discussion of the physical origins of these signals is given in Sec. IV A of [3].

The details of the calculation of $S_\omega(t)$ and $S_{2\omega}(t)$ are given in [3]; therefore only the most relevant equations needed for the magnetometric analysis are reproduced here. The magnetic resonance signals can be written as

$$S_\omega(t) = \mathcal{A}_0 h_\omega(\gamma)[D_\omega(\delta)\cos(\omega t-\alpha) - A_\omega(\delta)\sin(\omega t-\alpha)], \tag{1a}$$

$$S_{2\omega}(t) = \mathcal{A}_0 h_{2\omega}(\gamma)[-A_{2\omega}(\delta)\cos(2\omega t-2\alpha) - D_{2\omega}(\delta)\sin(2\omega t-2\alpha)], \tag{1b}$$

where $\mathcal{A}_0$ is the alignment, defined in [3], produced by the optical pumping. The angular dependencies of the first and second harmonic signals are given by

$$h_\omega(\gamma) = \frac{3}{16}(2\sin 2\gamma + 3\sin 4\gamma), \tag{2a}$$

$$h_{2\omega}(\gamma) = \frac{3}{32}(1 - 4\cos 2\gamma + 3\cos 4\gamma), \tag{2b}$$

where $\gamma$ is the angle between the light polarization and the static field $\boldsymbol{B}_0$. The first and second harmonic signals have both absorptive, $A_\omega(\delta)$, $A_{2\omega}(\delta)$, and dispersive, $D_\omega(\delta)$, $D_{2\omega}(\delta)$, components in their line shapes, given by

$$D_\omega(\delta) = \frac{\delta\Gamma_0\omega_1(\Gamma_2^2 + 4\delta^2 - 2\omega_1^2)}{Z(\delta)}, \tag{3a}$$

$$A_\omega(\delta) = \frac{\Gamma_0\omega_1[(\Gamma_2^2 + 4\delta^2)\Gamma_1 + \Gamma_2\omega_1^2]}{Z(\delta)}, \tag{3b}$$

$$D_{2\omega}(\delta) = \frac{\delta\Gamma_0\omega_1^2(2\Gamma_1 + \Gamma_2)}{Z(\delta)}, \tag{3c}$$

$$A_{2\omega}(\delta) = \frac{\Gamma_0\omega_1^2(\Gamma_1\Gamma_2 - 2\delta^2 + \omega_1^2)}{Z(\delta)}, \tag{3d}$$

with a resonance denominator,

$$Z(\delta) = \Gamma_0(\Gamma_1^2 + \delta^2)(\Gamma_2^2 + 4\delta^2) + [\Gamma_1\Gamma_2(2\Gamma_0 + 3\Gamma_2) - 4\delta^2(\Gamma_0 - 3\Gamma_1)]\omega_1^2 + (\Gamma_0 + 3\Gamma_2)\omega_1^4. \tag{4}$$

In Eqs. (3a)–(3d) and (4), $\omega_1 = \gamma_F B_1$ is the Rabi frequency of the rf field where $\gamma_F$ is the gyromagnetic ratio of the ground state hyperfine level $F$. The detuning $\delta = \omega - \omega_0$ is the difference between the rf frequency $\omega$ and the Larmor frequency $\omega_0 = \gamma_F B_0$, and $\Gamma_0, \Gamma_1, \Gamma_2$ are alignment relaxation rates. More precisely, the DRAM model [3] calculates the evolution of the alignment multipole moments $m_{2,q}$ via a density matrix approach (for a general introduction to the use of multipole moments in the density matrix formalism, see [10]). The moments $m_{2,q}$ are defined with respect to a quantization axis aligned with $\boldsymbol{B}_0$ and relax with rates $\Gamma_{|q|}$. In practice, both the absorptive $A_\omega(\delta)$, $A_{2\omega}(\delta)$, and dispersive, $D_\omega(\delta)$, $D_{2\omega}(\delta)$, components of the signals can be used to measure the magnetic field, and can be isolated by phase-sensitive detection of the transmission signals $S_\omega(t)$ and $S_{2\omega}(t)$.

The effect of $\gamma$, the angle between the linear polarization vector and the static magnetic field, is contained in the functions $h_\omega(\gamma)$ and $h_{2\omega}(\gamma)$. The first harmonic signal is maximized for $\gamma = 25.5°$ and the second harmonic signal for $\gamma = 90°$. Thus we distinguish between the following two realizations of the DRAM: (1) The first harmonic DRAM, choosing $\gamma = 25.5°$ and measuring $A_\omega(\delta)$ and $D_\omega(\delta)$, and (2) the second harmonic DRAM, choosing $\gamma = 90°$ and measuring $A_{2\omega}(\delta)$ and $D_{2\omega}(\delta)$.

Since the line shapes are different, we expect the two realizations of the DRAM to result in distinct optimum operating points and magnetometric sensitivities.

## III. EXPERIMENTAL SETUP

The experimental setup used for the optimization procedure is shown in Fig. 2. A Pyrex cell, paraffin-coated for spin relaxation suppression and evacuated except for an atomic cesium vapor in thermal equilibrium with a metal droplet, provided the paramagnetic atom sample. More details on the cell will be given in Sec. VIII. The cell was isolated from ambient magnetic fields by a three-layer $\mu$-metal shield (inner diameter 300 mm, length 580 mm, and outer diameter 590 mm). Inside the shield, a primary pair of Helmholtz coils

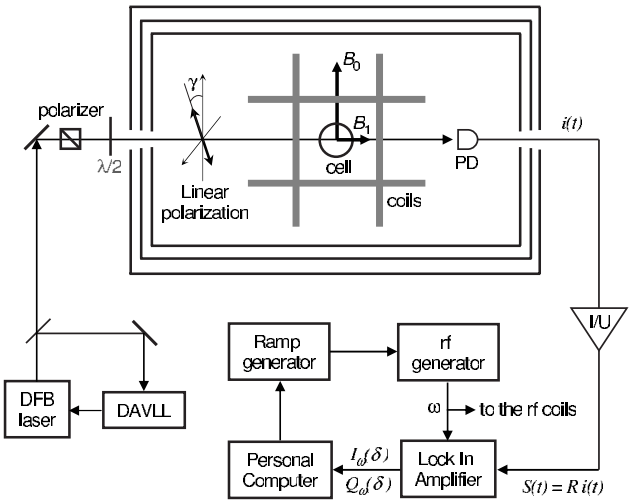


FIG. 2. Experimental setup: A cell containing Cs vapor was mounted inside a three-axis Helmholtz coil array all placed inside a three-layer $\mu$-metal shield. The polarization angle $\gamma$, measured with respect to the offset field $\boldsymbol{B}_0$, was set by a linear polarizer followed by a half-wave plate ($\lambda/2$) located outside the shield for ease of access. The laser light traversed the cell and was converted to a current by a nonmagnetic photodiode (PD). All details can be found in the text.

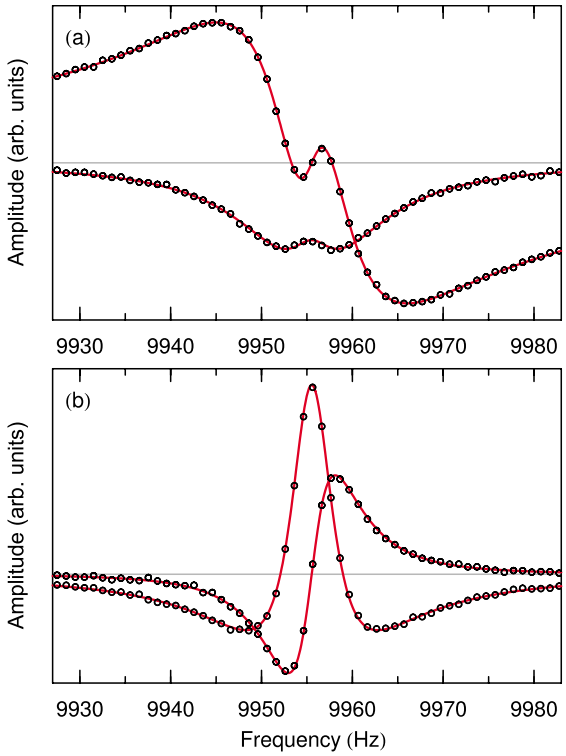


FIG. 3. (Color online) Measurements (circles) of the in-phase and quadrature magnetic resonance signals detected as amplitude modulations of the transmitted light power. (a) First harmonic signals. (b) Second harmonic signals. The statistical uncertainty on each data point is represented by the symbol size. The solid lines are fits of the theoretical line shapes given by Eqs. (3a) and (5b).

produced a static magnetic field $\boldsymbol{B}_0$ of about 3 $\mu$T perpendicular to the light propagation direction. Additional orthogonal pairs of Helmholtz coils (only one pair is shown in Fig. 2) were used to suppress residual fields and gradients. An rf magnetic field $\boldsymbol{B}_1$, rotating at approximately 10 kHz in the plane perpendicular to the static magnetic field, was created by a set of two pairs of Helmholtz coils, wound on the same supports as the static field coils. All internal structural components were made from nonmagnetic materials.

The laser beam (diameter $\approx$3 mm) used to pump and probe the atomic vapor confined in the cell was generated by a distributed feedback (DFB) diode laser, with a wavelength of 894 nm, stabilized to the $6S_{1/2}$, $F_g$=4$\rightarrow$$6P_{1/2}$, $F_e$=3 hyperfine transition by means of a dichroic atomic vapor laser lock (DAVLL) [11]. A linear polarizer followed by a half-wave plate prepared linearly polarized light of adjustable orientation $\gamma$ with respect to $\boldsymbol{B}_0$. The residual circular polarization contamination was measured to be less than 1%. A nonmagnetic photodiode, followed by a low-noise transimpedance amplifier, detected the light power transmitted through the cell. The resulting signal was analyzed by a lock-in amplifier tuned either to the first or second harmonic of the rf frequency, depending on the DRAM configuration under study (cf. Sec. II). A computer recorded magnetic resonance spectra by initiating the rf frequency sweep and simultaneously recording the in-phase and quadrature signals from the lock-in amplifier. The computer also controlled the light and rf power delivered to the cell and measured the total light power on the photodiode as well as the temperature of the apparatus. The system was thus automated and could make measurements of the magnetic resonance signals for ranges of light and rf powers. Forced air heating was used to make temperature changes to the system, changes that were slow with respect to the time needed to record one spectrum.

In practice, lock-in detection of the signals given by Eqs. (1a) and (1b) with respect to the rf frequency $\omega$ adds a phase $\phi_l$ (selectable in the lock-in amplifier) and a small pickup signal $p_{(1,2)(A,D)}$ (smaller than 1% of the signal at maximum) to each of the line shapes given by Eqs. (3a)–(3d) [4]. Due to $\phi_l$, the in-phase and quadrature spectra are, in general, a mixture of dispersive and absorptive line shapes. Demodulation of the signal Eq. (1a) yields expressions used to fit the recorded in-phase and quadrature spectra

$$I_\omega(\delta) = g_\omega(P_L)h_\omega(\gamma)\{[D_\omega(\delta)+p_{1D}]\cos(\alpha+\phi_l) + [A_\omega(\delta)+p_{1A}]\sin(\alpha+\phi_l)\}, \tag{5a}$$

$$Q_\omega(\delta) = g_\omega(P_L)h_\omega(\gamma)\{[A_\omega(\delta)+p_{1A}]\cos(\alpha+\phi_l) - [D_\omega(\delta)+p_{1D}]\sin(\alpha+\phi_l)\}. \tag{5b}$$

The $g_\omega(P_L)$ factor is used here to contain not only amplifier gain factors, but also the alignment $\mathcal{A}_0$ and any light power, $P_L$, dependencies. A similar mix of $A_{2\omega}(\delta)$ and $D_{2\omega}(\delta)$ was used for the second harmonic signal given by Eq. (1b).

Typical measured signals for the first and second harmonic magnetic resonance spectra are presented in Fig. 3, together with fits of the theoretical line shapes given by Eqs.

(3a) and (5b). All four curves are fitted simultaneously with one set of relaxation rates; for the presented data $\Gamma_0 = 2\pi \times 1.64(2)$ Hz, $\Gamma_1 = 2\pi \times 2.93(2)$ Hz, and $\Gamma_2 = 2\pi \times 3.08(2)$ Hz. Detailed information on the fitting procedure is found in [4]. The excellent quality of the fits allows us to extract the amplitude $g$, the relaxation rates $\Gamma_i$, and the Rabi frequency $\omega_1$ from a single set of double-resonance spectra. For that reason, no calibration of the rf coils is needed. This is an advantage compared to the DROM where the Rabi frequency and the longitudinal relaxation rate are correlated with the point where they cannot be individually extracted from measured line shapes.

## IV. MAGNETOMETRIC SENSITIVITY

The dispersive magnetic resonance line shapes given by Eqs. (3a) and (3c) have a linear dependence on the detuning $\delta = \omega - \gamma_F B_0$ at the center of the resonance. By proper choice of $\phi_l$, the quadrature signal, Eq. (5b), can be made completely dispersive, giving direct access to the linear zero crossing of the resonance,

$$Q_\omega(B_0) = g_\omega(P_L) h_\omega(\gamma) D_\omega(\omega - \gamma_F B_0), \tag{6}$$

with a similar expression for the $2\omega$ resonance. At constant $\omega$, $Q_\omega$ can be used as a magnetometer signal for a limited range of magnetic field strengths $|\omega - \gamma_F B_0| \ll \Gamma$, where $\Gamma$ is the resonance linewidth. In that range, a change of $B_0$ by a small $\Delta B_0$ can be measured as a change of $Q_\omega$ by the amount

$$\Delta Q_\omega = \Delta B_0 \left| \frac{dQ_\omega}{dB_0} \right|_{B_0 = \omega/\gamma_F} = \Delta B_0 t_\omega. \tag{7}$$

The slope $t_\omega$ is obtained from fits of the dispersive experimental magnetic resonance line shape (Fig. 3) using the relation

$$t_\omega = \left| \frac{dQ_\omega}{dB_0} \right|_{B_0 = \omega/\gamma_F} = \frac{-1}{\gamma_F} \left| \frac{dQ_\omega}{d\delta} \right|_{\delta = 0}. \tag{8}$$

Again, similar relations were used for the $2\omega$ signals.

The noise equivalent magnetic field (NEM) represents the noise limit on the derived value of $B$ given the noise in $Q$. The total noise in $Q$ has contributions from external magnetic field fluctuations and from all sources of technical noise, like laser intensity and frequency noise (converted to intensity noise by the atomic vapor), electronic noise, and so on. All technical noises can, in principle, be reduced until the system reaches the fundamental limit arising from the photocurrent shot noise. Therefore, we use the shot noise limited NEM as the measure for comparing the performance of different magnetometric schemes [1].

The root spectral density of the photocurrent shot noise is given by

$$\rho_S = R\sqrt{2eI_{\mathrm{dc}}}, \tag{9}$$

where $R$ is the transimpedance gain of the current amplifier, $e$ the electron charge, and $I_{\mathrm{dc}}$ the dc photocurrent. Given $\rho_S$, the NEM can be expressed as a root spectral density of field fluctuations by inverting Eq. (7)

$$\mathrm{NEM} = \frac{\rho_S}{|t_\omega|}. \tag{10}$$

Since $\rho_S$ was evaluated from a measurement of the photocurrent before the lock-in amplifier, the internal gain correction of the lock-in was used to give a measurement of $t_\omega$ usable in Eq. (10).

The goal of this study was to find the optimum DRAM operating parameters, $P_L$ and $\omega_1$, yielding maximum magnetometric sensitivity, i.e., minimal NEM.

## V. EMPIRICAL EXTENSION OF THE DRAM MODEL

As discussed in [3,4], the analytical expressions for the DRAM model [Eqs. (1a) and (4)] are valid for low laser power only; however, empirical formulas were presented modeling the light power dependence of the relaxation rates and of the global amplitude factors of the DRAM signals. Here, we present improved empirical formulas extending the DRAM model to even higher light powers, our goal being to cover the power domain that must be explored while optimizing the magnetometer.

The following empirical formula successfully represents the laser power dependence of the first harmonic signal,

$$g_\omega(P_L) = C \frac{P_L^2}{(P_{S1} + P_L)(P_{S2} + P_L)}, \tag{11}$$

where $C$ is a constant and $P_{S1}$, $P_{S2}$ are experimentally determined saturation powers for which we currently have no rigorous model in terms of fundamental physical constants and processes. A similar formula applies to the second harmonic amplitude, but requires different values for both the constant and the saturation powers. The model reflects the expectation that both the creation of alignment as well as the ability to probe the alignment will saturate with increasing power.

In a similar way, the $P_L$ dependence of the relaxation rates has been modeled by a power series, and good agreement with the measured data was found using a second order polynomial for each rate

$$\Gamma_0(P_L) = \Gamma_{00} + \alpha_0 P_L + \beta_0 P_L^2, \tag{12a}$$

$$\Gamma_1(P_L) = \Gamma_{10} + \alpha_1 P_L + \beta_1 P_L^2, \tag{12b}$$

$$\Gamma_2(P_L) = \Gamma_{20} + \alpha_2 P_L + \beta_2 P_L^2. \tag{12c}$$

We call the following parameter set the *extended DRAM model parameters*

$$\{C, P_{S1}, P_{S2}, \Gamma_{00}, \alpha_0, \beta_0, \Gamma_{10}, \alpha_1, \beta_1, \Gamma_{20}, \alpha_2, \beta_2\} \tag{13}$$

and note that they have to be determined experimentally. For that purpose, we have measured a series of double-resonance spectra as a function of laser power and extracted the amplitude and relaxation rates from the simultaneous fits, using common parameters, of the theoretical line shapes given by Eqs. (3a) and (5b) to the experimental data, as explained in [4]. The measurements were made separately for the first harmonic, with $\gamma = 25.5°$, and for the second harmonic, with

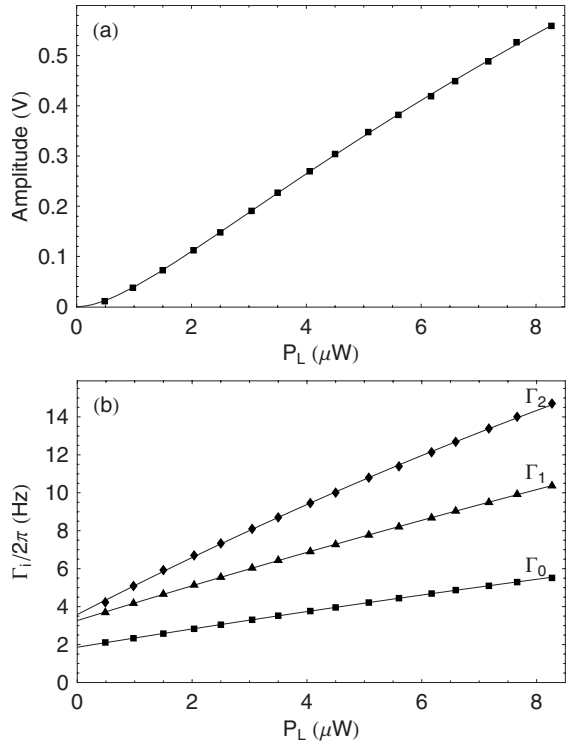


FIG. 4. (a) First harmonic DRAM signal amplitude as a function of laser power. (b) Relaxation rates as a function of laser power. Points are measured values, extracted from the fit of the DRAM model [Eqs. (3a)–(3d)] to the experimental magnetic resonance spectra. The solid lines are fits of the extended DRAM model [Eqs. (11) and (12a)–(12c)] to the experimental data. The data were measured at room temperature from a first harmonic DRAM with $\gamma = 25.5°$ and $\omega_1 = 2\pi \times 8.3$ Hz.

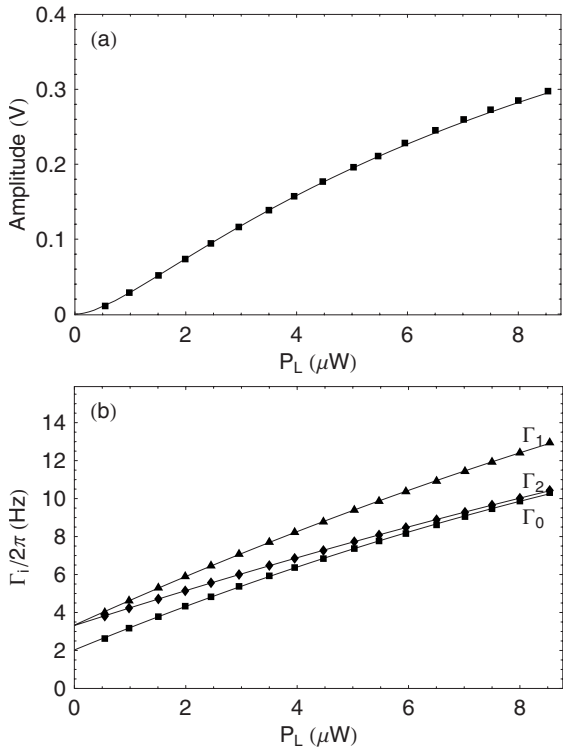


FIG. 5. (a) Second harmonic DRAM signal amplitude as a function of laser power. (b) Relaxation rates as a function of laser power. Points are measured values extracted from the fit of the DRAM model [Eqs. (3a)–(3d)] to the experimental magnetic resonance spectra. The solid lines are fits of the extended DRAM model [Eqs. (11) and (12a)–(12c)] to the experimental data. The data were measured at room temperature from a second harmonic DRAM with $\gamma = 90°$ and $\omega_1 = 2\pi \times 8.3$ Hz.

$\gamma = 90°$. The results are presented in Fig. 4 (Fig. 5) for the first (second) harmonic signals.

For determining $C$, $P_{S1}$, and $P_{S2}$, the empirical model of Eq. (11) was fitted to the amplitude data and the resulting fits are displayed as solid lines in the upper graphs of Figs. 4 and 5. To find the remaining extended parameters, $\Gamma_{00}$, $\Gamma_{10}$, $\Gamma_{20}$, $\alpha_0$, $\alpha_1$, $\alpha_2$, $\beta_0$, $\beta_1$, and $\beta_2$, the empirical model of Eqs. (12a)–(12c) was fitted to the $P_L$ dependence of the measured relaxation rates, and the resulting fits are displayed as solid lines in the lower graphs of Figs. 4 and 5. Clearly, the extended model accurately represents the data over the whole range of light powers investigated.

Table I summarizes the extended DRAM model parameters for both the first and the second harmonic signals. The expectation, based on the cylindrical symmetry of the physical system, that $\Gamma_{10}$ should equal $\Gamma_{20}$ is not reflected in the data, but the discussion of this will be delayed until Sec. VII.

## VI. PREDICTION OF THE DRAM OPTIMUM OPERATING POINT

### A. Description of the method

The optimum operating point of a DRAM can be predicted from the measured extended DRAM parameters presented in the preceding section. Here, the optimum operating point refers to the laser power $P_L$ and Rabi frequency $\omega_1$, which minimize the intrinsic NEM defined in Eq. (10). In

TABLE I. Experimental values of the extended DRAM model parameters extracted from the fits to the experimental data presented in Figs. 4 and 5. Only statistical uncertainties are shown. See text for details.

| Fit parameters | $\gamma = 25.5°$ | $\gamma = 90°$ |
|---|---|---|
| $C$ | 3.1(3) V | 1.0(2) V |
| $P_{S1}$ | 1.7(2) $\mu$W | 1.2(2) $\mu$W |
| $P_{S2}$ | 24(3) $\mu$W | 11(3) $\mu$W |
| $\Gamma_{00}/2\pi$ | 1.86(1) Hz | 2.03(3) Hz |
| $\Gamma_{10}/2\pi$ | 3.27(1) Hz | 3.34(2) Hz |
| $\Gamma_{20}/2\pi$ | 3.58(5) Hz | 3.31(1) Hz |
| $\alpha_0/2\pi$ | 0.492(4) Hz/$\mu$W | 1.21(1) Hz/$\mu$W |
| $\alpha_1/2\pi$ | 0.934(7) Hz/$\mu$W | 1.33(1) Hz/$\mu$W |
| $\alpha_2/2\pi$ | 1.55(3) Hz/$\mu$W | 0.946(4) Hz/$\mu$W |
| $\beta_0/2\pi$ | −5.6(5) mHz/$\mu$W$^2$ | −28(2) mHz/$\mu$W$^2$ |
| $\beta_1/2\pi$ | −8.9(9) mHz/$\mu$W$^2$ | −24(1) mHz/$\mu$W$^2$ |
| $\beta_2/2\pi$ | −26(3) mHz/$\mu$W$^2$ | −13.4(5) mHz/$\mu$W$^2$ |

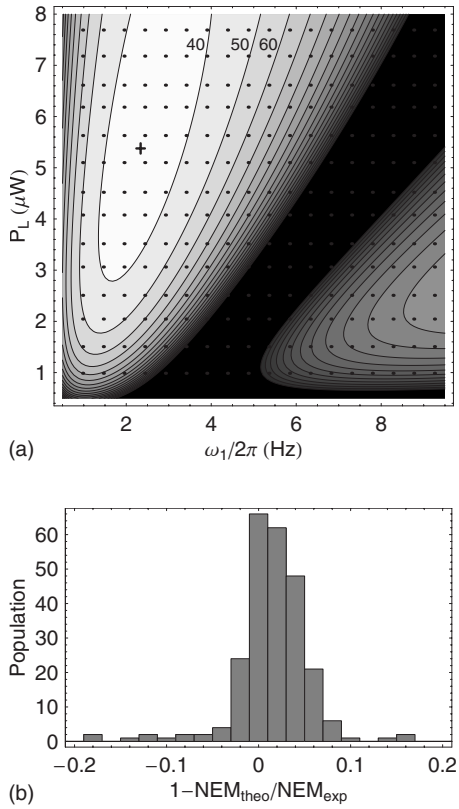


FIG. 6. First harmonic DRAM with $\gamma$=25.5°. The upper graph is a contour plot of the NEM as a function of $P_L$ and $\omega_1/2\pi$. The NEM values were calculated using the method developed in Sec. VI A. The cross indicates the position where the NEM is minimum (see Table II). The contour lines start at 40 fT/$\sqrt{\text{Hz}}$ and are spaced by 10 fT/$\sqrt{\text{Hz}}$. The dots indicate the points in parameter space where the NEM has been measured; cf. Sec. VI B. The distribution of the relative difference between calculated and measured values is shown in the lower graph.

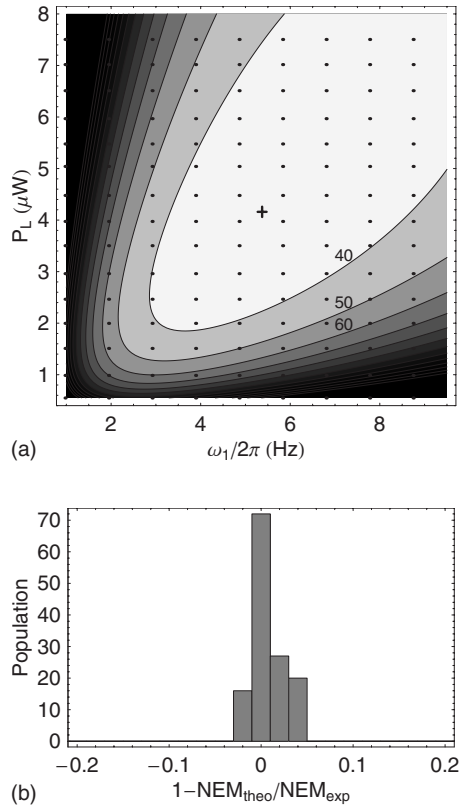


FIG. 7. Second harmonic DRAM with $\gamma$=90°. The upper graph is a contour plot of the NEM as a function of $P_L$ and $\omega_1/2\pi$. The NEM values were calculated using the method developed in Sec. VI A. The cross indicates the position where the NEM is minimum (see Table II). The contour lines start at 40 fT/$\sqrt{\text{Hz}}$ and are spaced by 10 fT/$\sqrt{\text{Hz}}$. The dots indicate the points in parameter space where the NEM has been measured; cf. Sec. VI B. The distribution of the relative difference between calculated and measured values is shown in the lower graph.

that equation, the photocurrent shot noise $\rho_s$ is calculated from the dc photocurrent using Eq. (9) and the on-resonance slope of the magnetometer signal is calculated from the derivative of the dispersive component of the resonance spectra; see Eqs. (6) and (8). By direct differentiation, we obtain

$$\left|\frac{dQ_\omega}{d\delta}\right|_{\delta=0} = \frac{g_\omega(P_L)h_\omega(\gamma)\Gamma_0(\Gamma_2^2-2\omega_1^2)\omega_1}{(\Gamma_1\Gamma_2+\omega_1^2)[\Gamma_0\Gamma_1\Gamma_2+(\Gamma_0+3\Gamma_2)\omega_1^2]} \quad (14)$$

for the slope of the first harmonic signal and

$$\left|\frac{dQ_{2\omega}}{d\delta}\right|_{\delta=0} = \frac{g_{2\omega}(P_L)h_{2\omega}(\gamma)\Gamma_0(2\Gamma_1+\Gamma_2)\omega_1^2}{(\Gamma_1\Gamma_2+\omega_1^2)[\Gamma_0\Gamma_1\Gamma_2+(\Gamma_0+3\Gamma_2)\omega_1^2]} \quad (15)$$

for the slope of the second harmonic signal. Combining the above with the power scaling model of Eqs. (11) and (12a)–(12c) and using the result in Eq. (10), the intrinsic NEM as a function of laser power $P_L$ and Rabi frequency $\omega_1$ is found.

This NEM function has been calculated for the extended DRAM model parameters given in Table I. The resulting contour plots of NEM as a function of $P_L$ and $\omega_1$ are presented in the upper graph of Fig. 6 for the first harmonic DRAM and in the upper graph of Fig. 7 for the second harmonic DRAM. Both graphs show a clear optimum point where the NEM is minimum. Table II lists the coordinates of these optimum points, together with the corresponding NEM value.

For the first harmonic DRAM, Fig. 6 shows a diagonal valley along $\omega_1=\Gamma_2(P_L)/\sqrt{2}$ where the NEM is maximized

TABLE II. Theory predictions of laser power $P_L$ and rf field Rabi frequency $\omega_1$ minimizing the NEM compared to the experimental best values. The calculations used the empirical extension of the DRAM model from Sec. V.

| DRAM scheme | Optimum $P_L$ ($\mu$W) | Optimum $\omega_1/2\pi$ (Hz) | NEM (fT/$\sqrt{\text{Hz}}$) |
|---|---|---|---|
| Theor. 1$\omega$ | 5.4 | 2.34 | 35.5 |
| Expt. 1$\omega$ | 5.1(2) | 2.40(5) | 35.7(7) |
| Theor. 2$\omega$ | 4.2 | 5.4 | 32.8 |
| Expt. 2$\omega$ | 4.5(2) | 5.6(1) | 32.6(6) |

(i.e., poor sensitivity). There, the NEM goes to infinity due to the onset of the narrow spectral feature (discussed in detail in [3]) appearing on the dispersive component of the resonance spectra, cf. Fig. 3(a), reducing the slope to zero.

### B. Verification of the method

The apparatus described in Sec. III was used to measure the on-resonance slope of the dispersive magnetic resonance signal. Then, that slope was inserted in Eq. (10) to determine the experimental value of the intrinsic NEM. We repeated the measurement on a $18\times14$ grid of $\omega_1$ and $P_L$ values for the first harmonic DRAM and a $9\times15$ value grid for the second harmonic DRAM. These measured points are shown as dots in the upper graphs of Figs. 6 and 7. For all measured points, the difference between the NEM predicted from the extended model and the measured value has been determined, and the distribution of the relative difference is plotted in the lower graph of Fig. 6 for the first harmonic DRAM, and in the lower graph of Fig. 7 for the second harmonic DRAM. Within the experimental uncertainty, there are no significant differences between the measurements and the predictions.

The experimental optimum operating points, where the measured NEM is minimized, was found, and the results are shown in Table II. Note that the optimal laser power is nearly the same for both first and second harmonic DRAMs. The Rabi frequency required to optimize the $2\omega$ NEM is more than twice that of the $1\omega$ NEM. The minimum NEM is slightly lower for the second harmonic signal. Table II compares the measured values with the predicted values calculated using the extended DRAM model. The agreement is very good, in particular for the NEM values. This means that given the relaxation rates and saturation powers, the optimum point can be predicted with precision of 5% using the extended DRAM model.

### C. Advantage of the method

The automated experimental determination of the optimum operating point of a DRAM, for a given temperature, can take several tens of hours. Indeed, that was the case for the NEM measurements over the grid of $P_L$ and $\omega_1$ values presented above.

By contrast, to find the optimum operating point based on the prediction of the extended DRAM model parameters requires only measurements as a function of $P_L$, since the $\omega_1$ dependence of the magnetic resonance spectra is perfectly described by the DRAM model presented in [3]. Thus the measurement time needed for finding the optimum can be reduced by one order of magnitude when using the above method to predict the optimum operating point instead of exploring the whole bidimensional parameter space. This is particularly useful for making a rapid characterization of the quality of coated Cs cells and when studying the optimum point as a function of temperature, the topic of the next section.

## VII. DRAM OPTIMUM POINT EVOLUTION WITH TEMPERATURE

The atomic vapor density and atom velocity distribution (and hence the interatomic and wall collision rates), as well as the relaxation probability during individual wall collisions, depend on temperature. The alignment relaxation rates, $\Gamma_0$, $\Gamma_1$, and $\Gamma_2$, depend in a nontrivial way on all those parameters because of three main contributing processes, namely collisional spin-exchange, wall collisions, and the reservoir effect [12–14]. Temperature thus has an important influence on the magnetometric sensitivity. Unfortunately, the influence is hard to model and so is worth measuring.

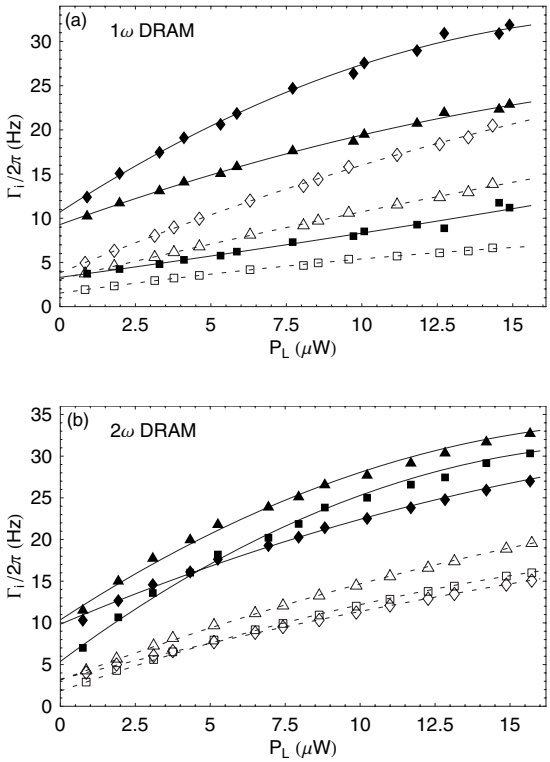


FIG. 8. Relaxation rates as a function of laser power, measured at two different temperatures. The empty symbols (□, △, ◇) represent $\Gamma_0,\Gamma_1,\Gamma_2$ measured at $T$=25 °C. The filled symbols (■, ▲, ◆) represent $\Gamma_0,\Gamma_1,\Gamma_2$ measured at $T$=38 °C. The solid and dashed lines are a fit of the extended DRAM model [Eqs. (12a)–(12c)] to the experimental data. (a) First harmonic DRAM with $\gamma$=25.5°. (b) Second harmonic DRAM with $\gamma$=90°.

The method developed in Sec. VI—predicting the optimum point from a measurement of the extended DRAM model parameters (cf. Sec. V)—was used to investigate the temperature dependence of the optimum DRAM operating point. Multiple measurements of the DRAM parameters were made for temperatures between 20 °C and 40 °C. As an illustration, the evolution of relaxation rates with temperature is shown in Fig. 8 where two measurements, at 25 °C and 38 °C, are presented. Even though the temperature evolution of the relaxation rates is nontrivial, the quadratic model of Eqs. (12a)–(12c) fits well to the experimental data and gives access to the relaxation rates $\Gamma_{00}$, $\Gamma_{10}$, and $\Gamma_{20}$ at zero light power. These parameters have been measured and their temperature behavior is presented in Fig. 9. They all increase with temperature, and this is mainly related to the increase of the atomic vapor density. During setup, we observed that the difference between $\Gamma_{10}$ and $\Gamma_{20}$ can be decreased by improving the magnetic field homogeneity, and

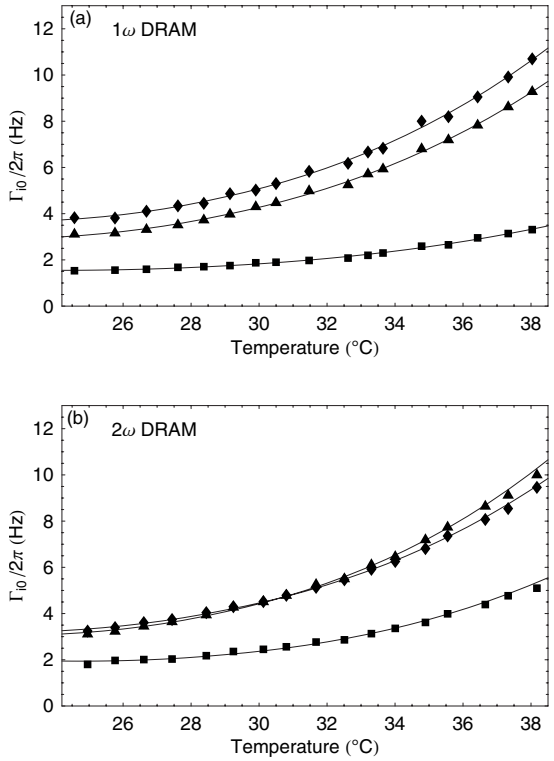


FIG. 9. Temperature evolution of the relaxation rates extrapolated to zero laser power. The symbols (■, ▲, ♦) represent $\Gamma_{00}, \Gamma_{10}, \Gamma_{20}$. The solid lines are fits of Eq. (16) to the experimental data. (a) First harmonic DRAM with $\gamma$=25.5°. (b) Second harmonic DRAM with $\gamma$=90°.

further tests confirmed that the difference between $\Gamma_{10}$ and $\Gamma_{20}$ increases with the square of the magnetic field inhomogeneity [15,16]. Moreover, the residual difference observed in our experiment is compatible with an estimation of the residual magnetic field inhomogeneity. This leads us to conclude that, in principle, the two transverse relaxation rates $\Gamma_{10}$ and $\Gamma_{20}$ should be equal in a perfectly homogeneous magnetic field. In Fig. 9, the solid lines are fits to the experimental data of the relaxation model given by

$$\Gamma_{i0} = n\sigma_i v_{\mathrm{rel}} + A v_m e^{E_a/kT} + B v_m + C v_m^{-1}. \qquad (16)$$

On the right-hand side, the first term is the contribution due to collisional spin-exchange: It is proportional to the vapor density $n(T)$, to the collisional disalignment cross section $\sigma_i$, and to the atoms' mean relative velocity $v_{\mathrm{rel}}(T) = \sqrt{16kT/(\pi M)}$, where $M$ is the $^{133}$Cs mass. The second term is the contribution due to wall collisions: It is proportional to the rate of wall collisions, hence to the atoms' mean velocity $v_m(T) = \sqrt{8kT/(\pi M)}$, and to the wall sticking time $\tau_s \sim \tau_0 e^{E_a/kT}$, where $\tau_0 \approx 10^{-12}$ s, $E_a$ is the adsorption energy, and $k$ is the Boltzmann constant. The third term is the contribution from the reservoir effect, and it is proportional to the rate of wall collisions and therefore to $v_m$. Finally, the last term is the contribution due to magnetic field inhomogeneities, which is proportional to $v_m^{-1}$ due to motional narrowing [16].

TABLE III. Collisional disalignment cross sections $\sigma_i$ obtained from the fit of Eq. (16) to the experimental data presented in Fig. 9. The last column gives the average of the values obtained for the $1\omega$ and $2\omega$ DRAMs. Errors are statistical only.

| Parameter | $1\omega$ DRAM | $2\omega$ DRAM | Average |
|---|---|---|---|
| $\sigma_0$ (cm$^2$) | $0.5(6)\times10^{-14}$ | $1.2(6)\times10^{-14}$ | $0.9(4)\times10^{-14}$ |
| $\sigma_1$ (cm$^2$) | $1.5(3)\times10^{-14}$ | $2.1(9)\times10^{-14}$ | $1.6(3)\times10^{-14}$ |
| $\sigma_2$ (cm$^2$) | $1.5(3)\times10^{-14}$ | $1.7(5)\times10^{-14}$ | $1.6(3)\times10^{-14}$ |

The vapor density $n(T)$ is calculated from the cesium vapor pressure given in [17]: It is highly temperature dependent. As a consequence, over the range of temperatures investigated in this work, the collisional spin-exchange term represents the main contribution to the temperature behavior of relaxation rates, and all other terms are approximately linear. Therefore, the fit is able to determine the Cs-Cs collisions disalignment cross sections $\sigma_i$, but cannot distinguish the contributions from the other terms with reasonable uncertainties. In principle, this can be improved by increasing the temperature range of the measurements and would lead to a powerful method for the investigation of relaxation mechanisms. However, at present, experimental setup cannot reach the necessary temperatures and so, since it is beyond the scope of the present paper, such investigations will be the subject of future work. The values of $\sigma_i$ extracted from the fits are summarized in Table III. These values have to be

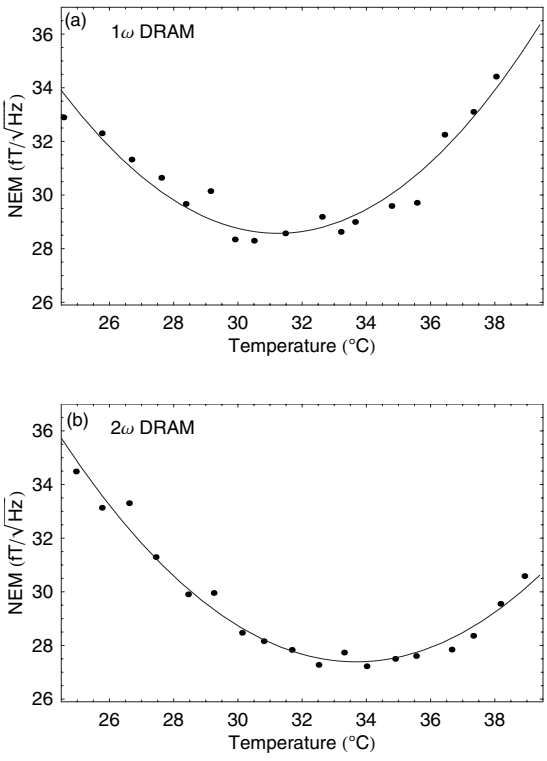


FIG. 10. Evolution of the optimum NEM as a function of temperature. (a) First harmonic DRAM with $\gamma$=25.5°. (b) Second harmonic DRAM with $\gamma$=90°. These graphs were calculated from the measurement of the extended DRAM model parameters.

TABLE IV. Results of the temperature NEM optimization procedure (as described in Sec. VII) applied to three different paraffin coated cells. Cell 1 was produced by our group; it is spherical with a 28 mm diameter. Cells 2 and 3 were purchased from a Russian company.

| | Cell 1 | Cell 2 | Cell 3 |
|---|---|---|---|
| Shape | Spherical | Cubic | Cylindrical |
| Volume $V$ | 11.5 cm$^3$ | 8.0 cm$^3$ | 4.6 cm$^3$ |
| Surface $S$ | 24.6 cm$^2$ | 24.0 cm$^2$ | 15.3 cm$^2$ |
| $V/S$ | 0.467 cm | 0.333 cm | 0.301 cm |
| | First harmonic DRAM | | |
| Optimum $T$ | 31.2 °C | 35.8 °C | 35.5 °C |
| Optimum $P_L$ | 6.2 $\mu$W | 12.1 $\mu$W | 5.2 $\mu$W |
| Optimum $\omega_1/2\pi$ | 2.9 Hz | 5.5 Hz | 4.8 Hz |
| Intrinsic NEM | 28.6 fT/$\sqrt{\text{Hz}}$ | 45.7 fT/$\sqrt{\text{Hz}}$ | 74.7 fT/$\sqrt{\text{Hz}}$ |
| | Second harmonic DRAM | | |
| Optimum $T$ | 33.7 °C | 36.2 °C | 37.6 °C |
| Optimum $P_L$ | 6.0 $\mu$W | 8.9 $\mu$W | 4.7 $\mu$W |
| Optimum $\omega_1/2\pi$ | 10.5 Hz | 14.1 Hz | 15.0 Hz |
| Intrinsic NEM | 27.4 fT/$\sqrt{\text{Hz}}$ | 39.3 fT/$\sqrt{\text{Hz}}$ | 62.2 fT/$\sqrt{\text{Hz}}$ |

taken with caution since the density used to infer the cross sections was taken directly from the Taylor-Langmuir formula [17], while it is known that the density in paraffin coated cells may deviate by up to 20% [13] from the expected thermal equilibrium value. A full exploration of the systematics arising from density effects, which depend on the cell used as well as parameters such as the applied light power and its resulting induced desorption [18], was beyond the scope of this work.

The extended DRAM model parameter measurements were used to calculate the evolution of the optimum operating point of the DRAM (cf. Sec. VI A). The results are presented, as a function of temperature, in Fig. 10 for both the first and second harmonic DRAMs. A quadratic polynomial was fitted to the NEM data in order to determine the temperature of minimum NEM. The experimental parameters characterizing these optimum points are summarized in the first column of Table IV, where we observe that the second harmonic DRAM is slightly more sensitive than the first harmonic DRAM.

## VIII. DISCUSSION

The majority of the work presented herein has been performed using a single evacuated Cs cell (cell 1 in Table IV). We applied the temperature NEM optimization procedure described in Sec. VII to two additional paraffin coated cesium cells and the resulting optimum parameters are presented in Table IV. The intrinsic NEM for the second harmonic DRAM is always smaller than for the first harmonic DRAM, and the lowest NEM value of 27.4 fT/$\sqrt{\text{Hz}}$ was obtained using the cell produced by our group (cell 1). We observe that the NEM values scale with the inverse of the volume of the cell and not with the volume to surface ratio. However, since the three cells do not have the same coating, this relation could be accidental.

Under identical conditions, the line shapes of the second harmonic DRAM signal are narrower than those of the DROM which, in principle, should lead to an improvement of the sensitivity [3]. Previous work by our group found an intrinsic sensitivity of 10 fT/$\sqrt{\text{Hz}}$ for an optimized DROM using a 70 mm diameter Cs vapor cell in the so-called $M_x$ configuration [19]. However, the experimental setup used in the past was very different (different cell size, offset field homogeneity, and magnetic shielding) and, in particular, the difference in cell dimensions disfavors the DRAM in this comparison. Therefore, a detailed comparative study is needed before drawing firm conclusions.

## IX. CONCLUSION

In conclusion, we have presented an experimental study of the intrinsic magnetometric sensitivity of the double-resonance alignment magnetometer, showing that an empirical extension of the DRAM model can be used to describe the magnetic resonance spectra over a range of experimental parameters sufficient for optimizing the magnetometer. A model has been developed to predict the optimum operating point of the magnetometer, i.e., the value of experimental parameters for which the magnetometric sensitivity is maximum. The method was verified by comparing its results to a direct measurement of the optimum operating point. In contrast to the time consuming direct optimization involving many hours of testing in a two parameter space, our method decreases the time required to find the optimum operation point to half an hour. Finally, we used this method to investigate the evolution of the optimum operating point of the DRAM with temperature, showing that the magnetometric sensitivity reaches an optimum of 27.4 fT/$\sqrt{\text{Hz}}$ for a

temperature of 33.7 °C. Both the first harmonic and the second harmonic realizations of the magnetometer were explored and compared. The temperature dependence of the relaxation rates yielded measurements of the Cs-Cs collisional disalignment cross sections of the tensor alignment, and the method promises to be useful in the continued study of the relaxation processes over broader temperature ranges.

## ACKNOWLEDGMENTS

This work was supported by grants from the Swiss National Science Foundation (Nos. 205321-105597 and 200020-111958), from the Swiss Innovation Promotion Agency, CTI (No. 8057.1 LSPP-LS), from the Swiss Heart Foundation, and from the Velux Foundation.

[1] G. Bison, R. Wynands, and A. Weis, J. Opt. Soc. Am. B **22**, 77 (2005).
[2] S. Groeger, G. Bison, and A. Weis, J. Res. Natl. Inst. Stand. Technol. **110**, 179 (2005).
[3] A. Weis, G. Bison, and A. S. Pazgalev, Phys. Rev. A **74**, 033401 (2006).
[4] G. Di Domenico, G. Bison, S. Groeger, P. Knowles, A. S. Pazgalev, M. Rebetez, H. Saudan, and A. Weis, Phys. Rev. A **74**, 063415 (2006).
[5] A. L. Bloom, Appl. Opt. **1**, 61 (1962).
[6] G. Bison, R. Wynands, and A. Weis, Opt. Express **11**, 904 (2003).
[7] W. Happer and B. S. Mathur, Phys. Rev. **163**, 12 (1967).
[8] J. P. Barrat and C. J. Cohen-Tannoudji, J. Phys. Radium **22**, 329 (1961).
[9] D. Budker, W. Gawlik, D. F. Kimball, S. M. Rochester, V. V. Yashchuk, and A. Weis, Rev. Mod. Phys. **74**, 1153 (2002).
[10] K. Blum, *Density Matrix Theory and Applications* (Plenum Press, New York, 1996).
[11] K. L. Corwin, Z.-T. Lu, C. F. Hand, R. J. Epstain, and C. E. Wieman, Appl. Opt. **15**, 3295 (1998).
[12] M. A. Bouchiat and J. Brossel, Phys. Rev. **147**, 41 (1966).
[13] V. Liberman and R. J. Knize, Phys. Rev. A **34**, 5115 (1986).
[14] D. Budker, L. Hollberg, D. F. Kimball, J. Kitching, S. Pustelny, and V. V. Yashchuk, Phys. Rev. A **71**, 012903 (2005).
[15] A. Abragam, *Principles of Nuclear Magnetism* (Oxford University Press, New York, 1961), reprint edition (2004).
[16] S. Pustelny, D. F. J. Kimball, S. M. Rochester, V. V. Yashchuk, and D. Budker, Phys. Rev. A **74**, 063406 (2006).
[17] J. B. Taylor and I. Langmuir, Phys. Rev. **51**, 753 (1937).
[18] E. B. Alexandrov, M. V. Balabas, D. Budker, D. English, D. F. Kimball, C.-H. Li, and V. V. Yashchuk, Phys. Rev. A **66**, 042903 (2002).
[19] S. Groeger, G. Bison, J.-L. Schenker, R. Wynands, and A. Weis, Eur. Phys. J. D **38**, 239 (2006).